/ The University of Electro-Communications

Net-Structure Proximity Sensor: High-Speed and Free-Form Sensor with Analog Computing Circuit

Net-Structure Proximity Sensor: High-Speed and Free-Form Sensor with Analog Computing Circuit

Hiroaki Hasegawa, Yosuke Suzuki, Aiguo Ming, *Member, IEEE,* Keisuke Koyama, Masatoshi Ishikawa, and Makoto Shimojo

Abstract—This paper proposes a proximity sensing system, which has advantages of wide sensing area and rapid response. For the rapid and safe behavior of robots, high-speed detection of nearby and non-contact objects is important because of shorter time-to-contact. Here, we propose Net-Structure Proximity Sensor (NSPS), which covers large sensing area and fulfills 1 millisecond response time. NSPS is an array of infrared reflective proximity sensor elements integrated by a resistor network circuitry. Executing analog computation on the electrical circuitry, the sensing system outputs a few of meaningful signals, from the reaction distribution of all the elements. The signals mean the center position and approximate distance to the object. This sensor requires only six external wires regardless of the number of detecting elements. In this paper, we firstly show that various sizes of NSPS are easily configured by only using standard electronic parts. Next, we prototype NSPS with 25 elements in 5×5 matrix, and verify the output characteristics by experiments. At last, we discuss the availability of NSPS for robot hand systems and human-machine interface systems.

Index Terms—Proximity sensor, optical sensor, photoreflector, mesh-structure, analog-circuitry, sensor integration.
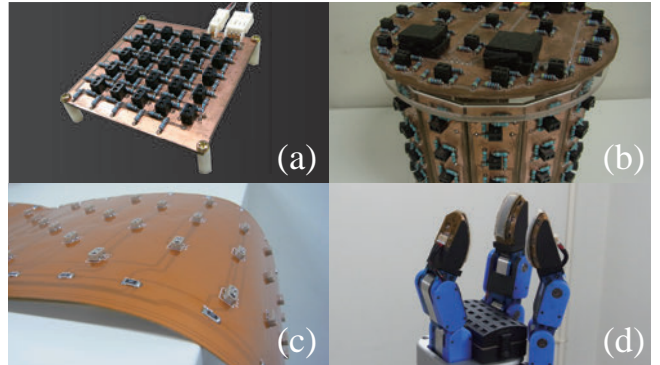

Fig. 1. Appearance of Net-Structure Proximity Sensors ((a) is a basic configuration on a plane, (b) is whole surface mounting on a cylindrical end-effector, (c) is the sensor on a flexible substrate for free-form surface, and (d) is a robot hand covered with the sensors on its palm and fingertips)

I. INTRODUCTION

ESSENCE of sensing for robotics is to provide useful information to determine the next motion of the robot. No matter how precise a sensor is, there is no worse if the obtained information cannot generate valuable control of the robot. Robot design should choose sensors in consideration of whether the amount of information, precision and measuring speed are appropriate for each stage of the target tasks or processes.

This paper proposes a high-speed proximity sensory unit using reflection of infrared light. This sensor unit contains multiple photo-sensor elements connected by an analog computing circuit. The large number of output signals are integrated into a small number of meaningful signals. The sensor can be mounted on a robot surface in free form with covering large area, and so the blind area can be reduced. The most important point is analog computation. It is carried out in the electrical circuitry based on the photo-current distribution of the elements. Due to the analog computation, the sensor unit provides valuable information for robot control, that is, there

H. Hasegawa, Y. Suzuki, A. Ming, K. Koyama and M. Shimojo are with the Department of Mechanical Engineering and Intelligent Systems, The University of Electro-Communications, Tokyo, 182-8585 Japan (e-mail: {hasegawa_hiro|koyama}@rm.mce.uec.ac.jp; {suzuki|ming|shimojo}@mce.uec.ac.jp).

M. Ishikawa is with the Department of Information Physics and Computing, Graduate School of Information Science and Technology, The University of Tokyo, Tokyo 113-8656, Japan (e-mail: ishikawa@k2.t.u-tokyo.ac.jp).

is no need for complicated information processing by CPU. Moreover, the computation time is independent on the number of the elements. We call the sensor unit as Net-Structure Proximity Sensor (NSPS), derived from the geometrical shape of the analog circuit, as shown in Fig. 1. The application fields of NSPS are robot hands to grasp unknown objects quickly and gently, and other robots to avoid collision with obstacles. NSPS is especially useful when there is not much time before contact with target objects, because it helps to determine the next motion of the robot in short time.

Generally, proximity sensors are used to cover marginal regions between detection ranges of vision sensors and tactile sensors. For manipulator systems, sensory-based control using proximity sensor feedback has been proposed since 1970s. Grippers mounting proximity sensors using infrared [1], [2] or ultrasound [3] were developed, and sensory-based robot control methods have been proposed [3], [4]. Recent researches showed object shape recognition based on surface tracking [5], [6], object tracking using electric-field proximity sensors mounted on a multifingered robot hand [7], [8], and reactive grasping controller combined with a probabilistic sensor model [9]. Other than these literatures, as Volpe and Ivlev mentioned in their survey [10], there are various kinds of detection methods such as infrared reflection (intensity, time-of-flight [11], triangulation [12]), ultrasound and capacitance [13].

Most of these sensors detects the distance to objects merely at a single point. Thus. if we apply these sensors to cover large area of surface of the robot such as robot hands, manipulators and whole body, we have to integrate a large

number of sensory output. The common solution is combining matrix-scanning method, embedded micro-controllers and field network. For tactile sensors, this kind of sensor system architectures to integrate a large number of taxels toward robotic skin are reported [14]–[16]. On the other hand, only a few works reported such a sensor system for proximity sensors. Lee et al. [13] devised 16×16 capacitive tactile-proximity sensor array. Ohmura et al. [17] developed a scalable tactile sensor skin, that is potentially applicable to proximity sensing because their sensor element detects applied force through light scattering in polyurethane foam by using photo-reflectors.

However, these common methods with matrix-scanning and field network are not suitable for the requirements of high-speed dynamic manipulation, because higher density layout of detectors requires more signal wires, data acquisition and processing time. This trade off makes it difficult for a robot system to behave fast and safely in a dynamic environment.

On the other hand, NSPS realizes both large surface covering and high update-rate for dynamic, high-speed sensor-based controlled robotics applications. Previously our group developed ultra high-speed grasping and manipulation system with 1000 frames-per-second high-speed active vision and Center-of-Pressure (CoP) tactile sensor. This system achieved sensory-based control at 1 millisecond control cycle and performed high-speed manipulation tasks such as pen-spinning [18], and gripping force adjustment to prevent the grasped object from slipping [19]. However, in these vision-tactile controlled manipulation tasks, occlusion that the robot itself hides the object to be manipulated was a major problem. Thus, we focused on the proximity sensor system with high update rate to match this control system.

The analog computation circuit of NSPS is very simple and easy to construct, which consists of resistors connecting the photo-elements and calculates the total amount and the center position of the photocurrent distribution. Here, each amount of photocurrent is mainly depending on the distance from the photo-sensor element to the nearest point on the object surface. Therefore, the output signal from NSPS indicates the positional relationship between the sensor and the object, and such information would be helpful for behavioral decision of the robots grasping the object.

The following chapters describe the structure and principle of NSPS, the meaning of the output from the sensor in a geometrical relationship between the sensor and the object, and experimental result to evaluate the detection characteristics of the prototyped sensor.

II. SENSOR STRUCTURE AND PRINCIPLE

A. Sensor structure

Net-Structure Proximity Sensor (NSPS) is an optical proximity sensor array integrated by two lattices of resistors. This sensor outputs two dimensional position and distance of a detected object. It has following features;

1) Requires only 4 readout wires.
2) Simple structure and small outline dimension.
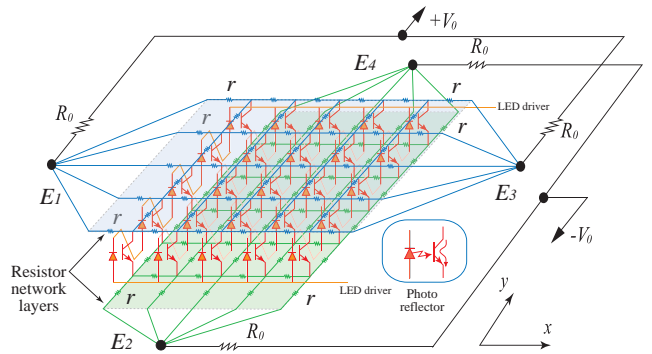3) Low-cost for large area covering application.

Fig. 2. Structure of the sensor; A detector layer is sandwiched by matrix arrayed resistor layers. Two resistor lattices, Layer A and B have the function to calculate primary moments of photocurrent distribution about x and y axis respectively. Four read-out electrodes (E_1, E_2, E_3 and E_4) are connected each side of the resistor lattices. This structure requires only 6 external wires; four to readout plus 2 to drive LEDs.

The structure of this circuit is shown in Fig. 2. It consists of three-layers similar to the mesh tactile sensor [20]: $m \times n$ photo-reflector array and two resistor network layers (Layer A and B).

A photo-reflector is a pair of an Infra-Red Light Emitting Diode (IR-LED) and a phototransistor. Its principle of proximity detection is based on reflection and decay of light emitted by IR-LEDs with distance to the object. Phototransistor detects the reflected IR and conducts relevant photocurrent. In our design, the arrayed photo-reflectors produce the photocurrent distribution corresponding to the shape, size, position and distance of the detected object.

Two resistor lattices, Layer A and B, have the function to calculate primary moments of photocurrent distribution about x and y axis in Fig. 2, respectively. In Layer A, collector terminals of neighboring phototransistors are connected by resistors r. In order to calculate the primary moment about the x-axis, electrodes E_1 and E_3 are placed on both ends of the resistor lattice. As shown in Fig. 2, electrode E_1 on the negative side in the x-axis is connected to the resistor lattice through r. This electrode is also connected to the positive voltage source $+V_0$ through an external resistor R_0. In the same manner, the positive side has the electrode E_3. In Layer B, emitter terminals of photoreflectors are connected by resistors r. The difference from Layer A is that Layer B is to calculate the primary moment about the y-axis, and the electrodes E_2 and E_4 are arranged on the both ends of the y-axis: Electrode E_2 is on the negative side, and electrode E_4 is on the positive one. In addition, they are connected to the negative voltage source $-V_0$ through external resistors R_0 respectively.

In this sensor structure, when the phototransistors detects IR, the currents from the positive voltage source $+V_0$ flow through the two electrodes E_1 and E_3 into Layer A, then flow through each phototransistors in response to detected irradiance, and finally flow out of Layer B through E_2 and E_4 to $-V_0$. From V_{S1}, V_{S2}, V_{S3} and V_{S4}, the voltages of the four electrodes, NSPS calculates the primary moments of the
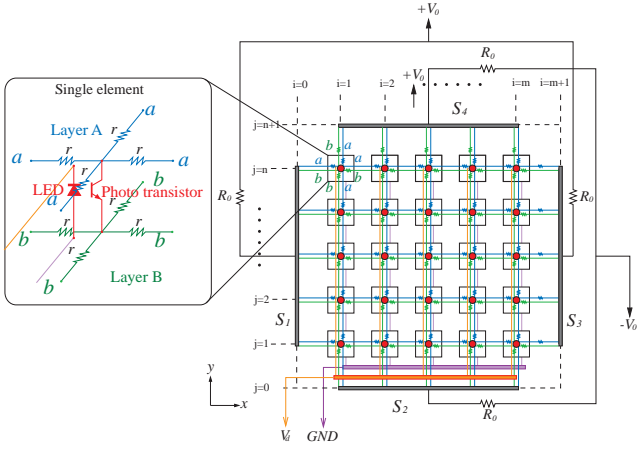
Fig. 3. Position of Detector Elements and Electrical Boundary Conditions of the Sensor.
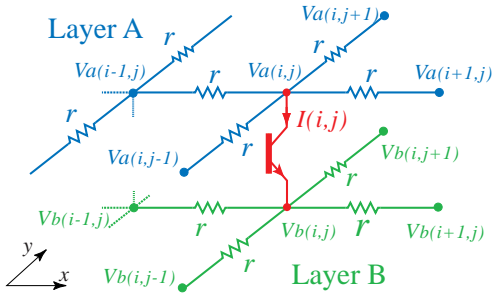

Fig. 4. Equivalent circuit at the neighborhood of a proximity sensor element (phototransistor)

photocurrent distribution. These parameters represent relative position between the sensor and a nearby object. The detailed principle of the operation is expressed in following sections.

B. Position Coordinates of the Detector Elements

The coordinate system and the indices i and j of the detectors are defined in Fig. 3. The detectors are placed on $m \times n$ grid, and a Cartesian coordinate system o-xy is defined as each corners of the grid has a coordinate $(x, y) = (1, 1), (-1, 1), (-1, -1), (1, -1)$ respectively. Each detector has its index (i, j); starting at the element placed $(x, y) = (-1, -1)$, $i = 1, 2, \ldots, m$ in x-axis direction, and $j = 1, 2, \ldots, n$ in y-axis direction. When the detector elements are placed at uniform intervals, the coordinate (x_e, y_e) of an element (i, j) is determined as below.

$$x_e(i,j) = \frac{2i - m - 1}{m - 1} \qquad y_e(i,j) = \frac{2j - n - 1}{n - 1} \quad (1)$$

As these equations form arithmetic progressions, equation (1) are represented using constants a, b, c, d.

$$x_e(i,j) = ai + b \qquad y_e(i,j) = cj + d \quad (2)$$

Applying this relationship, the Laplace operator becomes zero as shown in (3) and (4).

$$\begin{aligned}
\nabla^2 x_e(i,j) &= x_e(i-1,j) + x_e(i+1,j) \\
&\quad + x_e(i,j-1) + x_e(i,j+1) - 4x_e(i,j) \\
&= \{a(i-1)+b\} + \{a(i+1)+b\} \\
&\quad + \{ai+b\} + \{ai+b\} \\
&\quad - 4\{ai+b\} \\
&= 0 \quad (3)
\end{aligned}$$

$$\begin{aligned}
\nabla^2 y_e(i,j) &= y_e(i-1,j) + y_e(i+1,j) \\
&\quad + y_e(i,j-1) + y_e(i,j+1) - 4y_e(i,j) \\
&= \{cj+d\} + \{cj+d\} \\
&\quad + \{c(j-1)+d\} + \{c(j+1)+d\} \\
&\quad - 4\{cj+d\} \\
&= 0 \quad (4)
\end{aligned}$$

This relationship will be used in II-E.

C. Circuit and Basic Equation around the Detector Element

Figure 4 shows the circuit at the neighborhood of a detector element. The current flowing from Layer A (collector) to Layer B (emitter) through a phototransistor (i, j) is set to $I(i, j)$. The voltage $V_a(i, j)$ and $V_b(i, j)$ are the voltage of the corresponding nodes on layers A and B. Applying Kirchhoff's current law on the Layer A, $I(i, j)$ has following relationship.

$$\begin{aligned}
\frac{1}{r}\{V_a(i-1,j) + V_a(i+1,j) + V_a(i,j-1) \\
+ V_a(i,j+1) - 4V_a(i,j)\} = I(i,j) \quad (5)
\end{aligned}$$

Replacing the left hand side of (5) with the discrete Laplace operator ∇^2 in (6), it can be written as (7).

$$\begin{aligned}
\nabla^2 V_a(i,j) &= V_a(i-1,j) + V_a(i+1,j) \\
&\quad + V_a(i,j-1) + V_a(i,j+1) - 4V_a(i,j) \quad (6)
\end{aligned}$$

$$\frac{1}{r}\nabla^2 V_a(i,j) = I(i,j) \quad (7)$$

In the same manner, the following equation can be derived for Layer B;

$$\frac{1}{r}\nabla^2 V_b(i,j) = -I(i,j) \quad (8)$$

D. Boundary Conditions of Resistor Network

Considering the electrical boundary conditions of the sensor structure shown in Fig. 3, the boundaries S_2 and S_4 of Layer A do not have any external connections so that these are open terminals. Hence, no current flows from outside and the voltage does not change. The boundary conditions therefore are shown, as in (9).

$$V_a(i,0) = V_a(i,1) \qquad V_a(i,n+1) = V_a(i,n) \quad (9)$$

Next, the boundaries S_1 and S_3 of Layer A are connected to the electrode E_1 and E_3, respectively, such that current flows from the electrodes. This current passes through the external resistor R_0. Hence, this current can be measured from the

voltage drop between the ends of R_0. Since the total of the current that passes through the detectors is equal to the current that flows through R_0, (10) and (11) are established as follows;

$$\frac{1}{R_0}\left(V_0 - V_{S1}\right) = \frac{1}{r}\sum_{j=1}^{n}\left(V_{S1} - V_a(1,j)\right) \tag{10}$$

$$\frac{1}{R_0}\left(V_0 - V_{S3}\right) = \frac{1}{r}\sum_{j=1}^{n}\left(V_{S3} - V_a(m,j)\right) \tag{11}$$

Since $i = 0$ for the electrode E_1 and $i = m+1$ for the electrode E_3, boundary conditions are as;

$$V_a(0,j) = V_{S1} \qquad V_a(m+1,j) = V_{S3} \tag{12}$$

Layer B situated similarly, the boundary conditions for this layer are established as (13) - (16).

$$V_b(0,j) = V_b(1,j) \qquad V_b(m+1,j) = V_b(m,j) \tag{13}$$
$$V_b(i,0) = V_{S2} \qquad V_b(i,n+1) = V_{S4} \tag{14}$$

$$\frac{1}{R_0}\left(-V_0 - V_{S2}\right) = \frac{1}{r}\sum_{i=1}^{m}\left(V_{S2} - V_b(i,1)\right) \tag{15}$$

$$\frac{1}{R_0}\left(-V_0 - V_{S4}\right) = \frac{1}{r}\sum_{i=1}^{m}\left(V_{S4} - V_b(i,n)\right) \tag{16}$$

E. Primary Moment of Photocurrent

To determine the center of the photocurrent distribution of the $m \times n$ detectors, it is necessary to determine the primary moments of the photocurrent distribution with respect to the x and y direction. In the x direction, the primary moment I_x is defined as (17).

$$I_x = \sum_{i=1}^{m}\sum_{j=1}^{n} I(i,j)x_e(i,j) \tag{17}$$

Substituting (17) for the current $I(i,j)$ gives (18), then the equation can be deformed as (19) by expanding the Laplace operator ∇^2.

$$I_x = \frac{1}{r}\sum_{i=1}^{m}\sum_{j=1}^{n} x_e(i,j)\nabla^2 V_a(i,j) \tag{18}$$

$$= \frac{1}{r}\left\{ \sum_{i=1}^{m}\sum_{j=1}^{n} V_a(i,j)\nabla^2 x_e(i,j) \right.$$
$$+ \sum_{j=1}^{n}\Big(x_e(m,j)V_a(m+1,j) - x_e(m+1,j)V_a(m,j) \Big)$$
$$+ \sum_{j=1}^{n}\Big(x_e(1,j)V_a(0,j) - x_e(0,j)V_a(1,j) \Big)$$
$$+ \sum_{i=1}^{m}\Big(x_e(i,n)V_a(i,n+1) - x_e(i,n+1)V_a(i,n) \Big)$$
$$\left. + \sum_{i=1}^{m}\Big(x_e(i,1)V_a(i,0) - x_e(i,0)V_a(i,1) \Big) \right\} \tag{19}$$

Next, let us apply the position coordinates and the boundary condition for simplifying (19). The first item of (19) becomes

zero by (3). Since $x_e(i,j)$ is the function of only i, it is constant toward the direction of j, that is, $x_e(i,n) = x_e(i,n+1)$, $x_e(i,0) = x_e(i,1)$. Coupled with the boundary condition given by (9), the fourth and fifth items also become zero. Furthermore, applying the boundary conditions (10), (11) and (12), (19) can be simplified as below.

$$I_x = \frac{1}{r}\left\{ \sum_{j=1}^{n}\Big(1 \cdot V_a(m+1,j) - \frac{m+1}{m-1}V_a(m,j) \Big) \right.$$
$$\left. + \sum_{j=1}^{n}\Big(-1 \cdot V_a(0,j) + \frac{m+1}{m-1}V_a(1,j) \Big) \right\} \tag{20}$$

$$= \frac{n}{r}V_{S3} - \frac{m+1}{m-1}\left\{ \frac{n}{r}V_{S3} - \frac{1}{R_0}(V_0 - V_{S3}) \right\}$$
$$- \frac{n}{r}V_{S1} + \frac{m+1}{m-1}\left\{ \frac{n}{r}V_{S1} - \frac{1}{R_0}(V_0 - V_{S1}) \right\} \tag{21}$$

$$= \frac{1}{n-1}\left(\frac{2m}{r} + \frac{n+1}{R_0} \right)(V_{S1} - V_{S3}) \tag{22}$$

Similarly I_y, the primary moment with respect to the y direction, is expressed as (23).

$$I_y = \frac{1}{m-1}\left(\frac{2n}{r} + \frac{m+1}{R_0} \right)(V_{S2} - V_{S4}) \tag{23}$$

F. Total Current and Center of Current Distribution

The total current I_{all} flowing from Layer A to Layer B can be calculated by adding two currents flowing through a pair of external resistors R_0 of Layer A or Layer B by (24).

$$I_{all} = \sum_{i=1}^{m}\sum_{j=1}^{n} I(i,j)$$
$$= \frac{(2V_0 - V_{S1} - V_{S3})}{R_0} = \frac{(2V_0 + V_{S2} + V_{S4})}{R_0} \tag{24}$$

With the above, the centers of the current distribution x_c and y_c are determined as

$$x_c = \frac{I_x}{I_{all}}$$
$$= \frac{R_0}{n-1}\left(\frac{2m}{r} + \frac{n+1}{R_0} \right)\frac{V_{S1} - V_{S3}}{2V_0 - V_{S1} - V_{S3}} \tag{25}$$

$$y_c = \frac{I_y}{I_{all}}$$
$$= \frac{R_0}{m-1}\left(\frac{2n}{r} + \frac{m+1}{R_0} \right)\frac{V_{S2} - V_{S4}}{2V_0 + V_{S2} + V_{S4}}. \tag{26}$$

Here, m, n, r, R_0 and V_0 are constants. Hence, I_{all}, x_c and y_c can be computed by only measuring the voltages on the four electrodes E_1, E_2, E_3 and E_4.

III. REPRESENTATION OF SENSOR OUTPUTS

In this section, let us look into the relationship between the current distribution of the photo-reflectors and the position of the detected object. As we mentioned, the NSPS outputs the center position and the total amount of the current distribution from the four electrodes. This current distribution is derived

from the irradiance of infrared rays detected by each phototransistors. In reflective photo sensors, the output current is inversely proportional to the square of the distance to the detected object. We examine the meaning of the center position output of this kind of sensor.

A. Center of the photocurrent distribution

Figure 5 shows the arrangement of the sensor and a detected object. When NSPS on x-y Plane detects an object in $z \geq 0$ region, the distribution of photocurrent $I(x, y)$ is written as follows over the domain D; orthographic projection of the outline of the object.

$$I(x, y) = k \cdot d(x, y)^{-2} \tag{27}$$

where $d(x, y)$ is the perpendicular length between the object and the coordinate $(x, y, 0)$, and k is a constant determined by the reflectance of the object and the sensitivity of the detector. To simplify the discussion, assuming the arrangement of the detector elements is dense enough, we approximate the summation of the photocurrent distribution by double integral. Under this assumption, the primary moments I_x, I_y and the total current I_{all} are expressed as

$$I_{all} = \iint_D I(x, y) \mathrm{dxdy} = \iint_D kd(x, y)^{-2} \mathrm{dxdy} \tag{28}$$

$$I_x = \iint_D x \cdot I(x, y) \mathrm{dxdy} = \iint_D x \cdot kd(x, y)^{-2} \mathrm{dxdy} \tag{29}$$

$$I_y = \iint_D y \cdot I(x, y) \mathrm{dxdy} = \iint_D y \cdot kd(x, y)^{-2} \mathrm{dxdy} \tag{30}$$

In the case of Fig. 5, a sphere with the center coordinates (x_o, y_o, z_o) and the radius R is placed in front of detector plane. The surface of the sphere and the distance from the detectors to object is formulated as

$$(x - x_o)^2 + (y - y_o)^2 + (z - z_o)^2 = R^2 \tag{31}$$

$$d(x, y) = z_o - \zeta \tag{32}$$

$$\zeta = \sqrt{R^2 - (x - x_o)^2 - (y - y_o)^2}. \tag{33}$$

In this situation, the integration domain is

$$D = \left\{ (x, y) | (x - x_o)^2 + (y - y_o)^2 \leq R^2 \right\}. \tag{34}$$
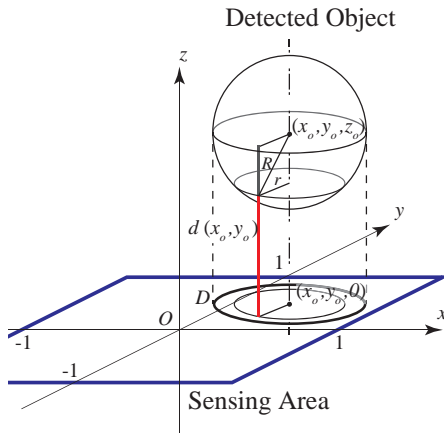
Detected Object

Fig. 5. Relationship between Position Output of NSPS and Object Positioning

From (27), the photocurrent is represented as

$$I(x, y) = k \cdot d(x, y)^{-2} = k \cdot (z_o - \zeta)^{-2} \tag{35}$$

By applying integration by parts, the total current and the primary moments are calculated as

$$I_{all} = \iint_D k \cdot d(x, y)^{-2} \mathrm{dxdy} \tag{36}$$

$$= \iint_D \frac{-k\zeta}{(z_o - \zeta)^2} \mathrm{d}\theta \mathrm{d}\zeta$$

$$= 2\pi k \int_0^R \zeta(z_o - \zeta)^{-2} \mathrm{d}\zeta$$

$$= 2\pi k \left[\zeta(z_o - \zeta)^{-1} \right]_0^R - 2\pi k \int_0^R (z_o - \zeta)^{-1} \mathrm{d}\zeta$$

$$= \pi R^2 k \left\{ \frac{2}{R(z_o - R)} + \frac{2}{R^2} \log \frac{z_o - R}{z_o} \right\} \tag{37}$$

$$I_x = \iint_D x \cdot kd(x, y)^{-2} \mathrm{dxdy}$$

$$= \iint_D (x_o + r \sin \theta) \cdot kd(x, y)^{-2} r \mathrm{d}\theta \mathrm{d}r$$

$$= \iint_D x_o kd(x, y)^{-2} r \mathrm{d}\theta \mathrm{d}r$$

$$+ \iint_D r^2 \sin \theta kd(x, y)^{-2} \mathrm{d}\theta \mathrm{d}r$$

$$= x_o I_{all} + 0. \tag{38}$$

From these results, the position output of NSPS is represented as

$$x_c = \frac{I_x}{I_{all}} = x_o \qquad y_c = \frac{I_y}{I_{all}} = y_o. \tag{39}$$

Thus, (x_c, y_c) stands for the center position of the detected object, and the total current I_{all} indicates the distance of the object providing the size is constant.

Through a simple example, we denoted the primary moments of photocurrent are determined by the position of the detected object. This relation enables NSPS to detect the position and distance of the object from the primary moment and total of photocurrent.

In the above example, we assumed the following conditions.
1) The object has a symmetrical shape, and the whole of the projection is inside of the sensing area.
2) The reflection is perfect diffuse reflection, and the reflection ratio is equal in all the object surface.
3) The directivity of the elements is sufficiently high. (The half-value angle is sufficiently small.)

Actually equipped sensors have different characteristics due to difference with these conditions. However, the characteristics can be predicted and controlled theoretically. In the next section, we show a prototyped NSPS and its output characteristics.

IV. DESIGN AND PROTOTYPING OF THE SENSOR

In this section, we describe a prototype design of NSPS. This sensor consists of an array of photo-reflectors, two resistor network layers and amplifier which calculates from (24)–(26). We designed these components then fabricated a prototype of NSPS with 5×5 elements shown in Fig.6.

A. Detection Characteristics of Photoreflectors

We applied RPR-220 (manufactured by ROHM Co., Ltd.) as the photo-reflectors because of its long detection range, availability of device and easy mounting on printed circuit board (PCB) for prototyping. The basic specification of RPR-220 is shown in Fig. 6. In this case, 25 photo-reflectors are required for constructing 5×5 NSPS, but individual variability of the photo-reflectors may lead to the bias of the position output and degrade the output accuracy. Thus, we conducted a preliminary test and selected the photo-reflectors within ± 0.1 mA difference of peak photocurrent and ± 2.0 mm difference of peak sensitivity distance.

B. Arrangement of Detector Elements

In this prototype design, the detector elements are arranged in a rectangular pattern with 20-mm pitch. For more practical detection performance, we have to optimize the arrangement of the detectors from the design considerations such as maximal detection distance, directionality of the detector element, size of the detected objects and shape of the sensor attached surface. It should be useful to employ the simulation-based optical design using ray-tracing method as described in [21].

C. Parameters of Resistor Network

Next, we designed the parameters of the resistors r and R_0 considering the specification of the prototype and RPR-220 photo-reflector. From the input voltage range of ADC (bipolar ± 10 V), the power supply of the circuit including both amplifier and sensor is ± 12 V, and the reference voltage $\pm V_0$ for NSPS is ± 6 V. Here, the resistance values r and R_0 determine the output ranges of the electrode voltages $V_{S1} \sim V_{S4}$. For matching them to the amplifier design described below, we selected $r = 1000\Omega$ and $R_0 = 620\Omega$.

D. Amplifier

We designed an amplifier circuit which has following two functions. The first is to calculate the differential voltages between the electrodes and the total current of the NSPS circuit. The second is to magnify the output signals to the proper voltage range for data acquisition.
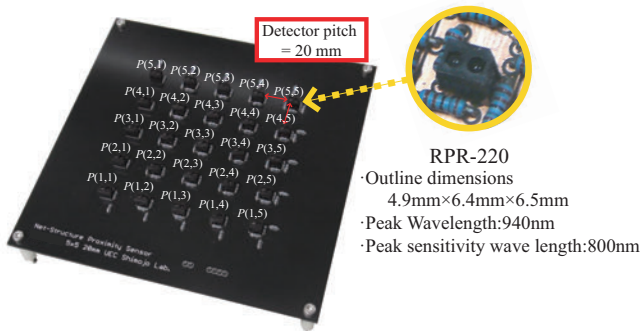

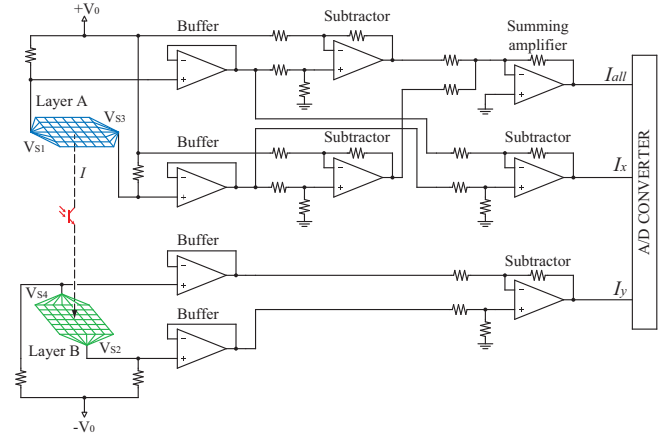Fig. 6. Prototype 5×5 Net-Structure Proximity Sensor

Fig. 7. Schematic of the Amplifier Circuit for calculating I_{all}, I_x and I_y from the electrode voltages V_{S1}, V_{S2}, V_{S3} and V_{S4}
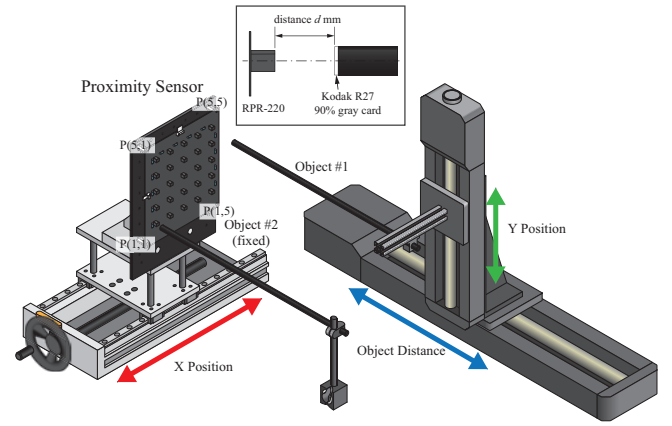

Fig. 8. Experimental Setup; Three lead-screw linear stages changes relative position between the NSPS under the test and teaget objects. The sensor was mounted on Misumi KUE14-A-320 manual linear motion unit (X-axis), the detected object #1 was positioned by Sigma Koki motorized linear stages; SGSP-33-200 (Y-axis) and SGSP46-500 (Z-axis) respectively.

Figure 7 shows the design using operational amplifier based circuit with three stages. On the first stage, buffers are interposed to keep latter stages from interfering the operation of resistor network. The second stage calculates the voltage drops by two external resistors R_0. The last stage has a summing amplifier with inputs from results of the second stage $(V_{S1} - V_0)$ and $(V_{S3} - V_0)$ for calculating I_{all} output, and two differential amplifiers subtract between the pairs of opposite electrodes for calculating I_x and I_y output respectively.

V. EXPERIMENTS ON DETECTION PERFORMANCE

We evaluated object detection characteristics of the prototype through some experiments. The experimental setup is shown in Fig. 8, where our sensor and an object to be detected were mounted on three linear stages (Y and Z-axis; Sigma Koki SGSP Series, X-axis; a manual lead-screw stage). The target object is $\phi 12$ mm of white board (Kodak R27 90% gray card.) To avoid reflection by other devices such as the linear stages and the table, the target was mounted at the end of black polyacetal sticks (diameter = 12 mm, length = 200 mm).
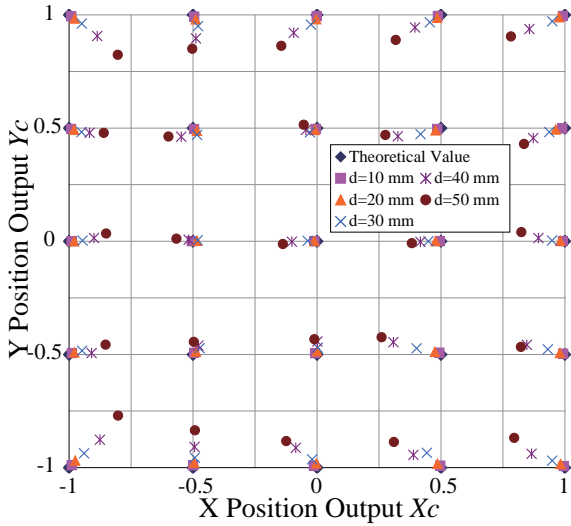
Fig. 9.   Position output response directly upon detector elements.

Fig. 10.   Distance output response.

Each LED was applied forward current $I_f = 40$ mA. The output signals from the amplifier were measured by National Instruments PXI-6251 analog-to-digital converter at the settings of 16-bit bipolar ± 10 V, sampling rate 10 kHz. Prior to the experiment we measured initial output without any target object to compensate some errors caused by following factors.

- IR crosstalk within photoreflector packages.
- Photocurrent induced by environmental light source.
- Output voltage offset error of operational amplifiers.

Then from the measured signals the differential voltages $V_{S1} - V_{S3}$ and $V_{S2} - V_{S4}$ were calculated, and substituted for (24)–(26) to obtain the position of the object (x_c, y_c) and the total current I_{all}.

A. Position Measurement Performance

We investigated the relation between the position of a detected object and the output of the prototype sensor. In this experiment, a target is placed in front of one of the detector elements, changes of position output x_c and y_c by distance between the surface of the element and the target d [mm] are recorded respectively. The results are shown in Fig. 9. Within $d = 30$ mm, the position output (x_c, y_c) properly represents the place of the photoreflector elements on the sensor plane. With more distant targets, the position output tends to move toward the center of the sensor. This is caused by the directivity of the photo-elements. A part of radially emitted/reflected light goes out of the sensing area, and so the position output shifts toward the center compared to the position just below the object.

B. Distance Measurement Performance

Next we investigated the distance output. The total current I_{all} was measured while the target was placed in front of the element $P(3,3)$, and moved away from it. We tested the distance d from 0 mm (the target contacts on the top surface of
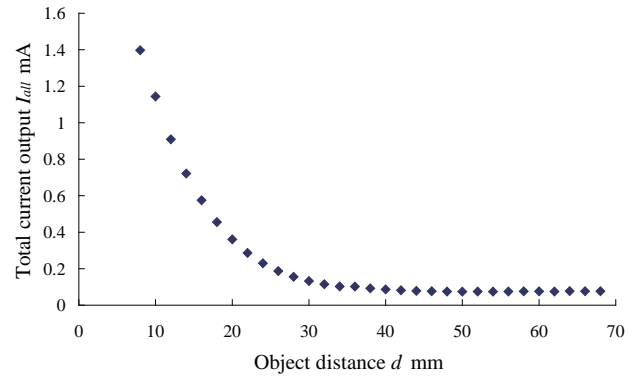
RPR-220) to 70 mm. Figure 10 shows the relationship between the total current I_{all} mA and the distance to the target d mm. I_{all} decayed approximately inversely proportionally of the square of the distance. We can see that this sensor is capable to performs the distance measurement within $d = 40$ mm from the change of I_{all}.

C. Transient Response

Finally we tested the transient response of the sensor. To investigate the response in worst case, the LEDs were driven by a step input of forward current $I_f = 10$ mA and the target was faced the detector element $P(3,3)$ at 6 mm distance. The response of I_{all} was measured as shown in Fig. 11. LEDs are turned on or off at the time $t = 1$ ms. In these waveforms, the rise time and fall time of the total current output I_{all} to 95% are 0.424 ms and 0.380 ms, respectively. The results shows that the design of out prototype satisfied 1 ms response time in case of both approaching and leaving objects.

VI. DISCUSSIONS

The experimental results in the last section showed that the position outputs (x_c, y_c) correspond to the object position along the sensor surface, and the total current I_{all} changes according to the distance from the sensor to the object. In this section, we discuss the points to be considered before designing an actual NSPS.

Firstly, about the position output, it was shown that the characteristic changes according to the distance from the sensor to the object caused by the directivity of the photoreflectors. The more obtuse the directivity is, the more widely the phototransistors react, and some of the emitted light leaks out of the sensing area. The effect becomes significant at larger distance. Although the the directivity of RPR-220 is 10 degrees in half-value angle, which is sharper than similar products, the effect is hard to be ignored as shown in Fig. 9. However, since the degree of the effect can be predicted by the theory of reflection, it does not necessarily degrade the accuracy of NSPS.

On the other hand, there is a merit when the directivity is obtuse that each photo-element detects wide area. That is,
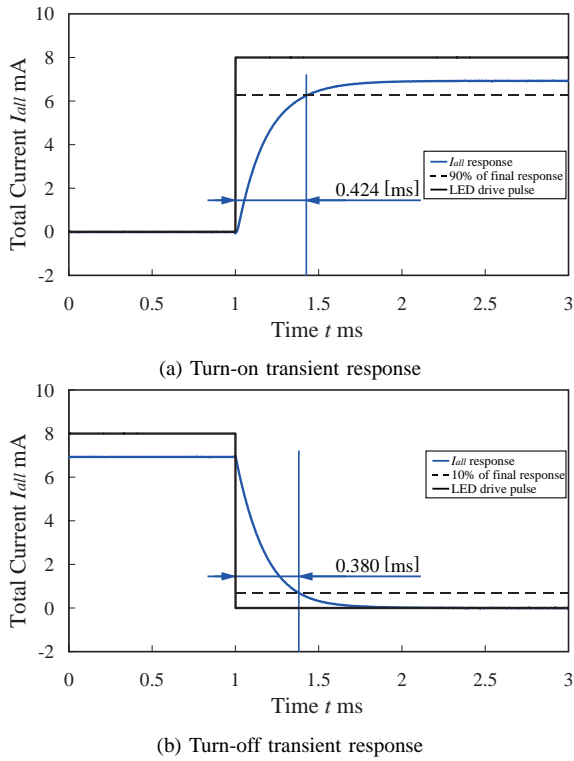
(a) Turn-on transient response

(b) Turn-off transient response

Fig. 11.   Step response of I_{all} at LED turn-on and turn-off

(a) Overview of the Human interface application of NSPS

(b) Circular Trajectory   (c) Spiral Trajectory

Fig. 12.   Human Interface Application and Examples of Captured Trajectories

we can arrange the elements more sparsely without any dead region. Although NSPS has an advantage that the number of elements affects neither the sensing speed nor the external wiring, reduction of the elements helps to cut production cost and to design a total robot system with less structural constraint. Therefore, we should choose a photo-element which has proper characteristics for the required detection range and the mechanical design of the target robot system.

Secondly, about the total current, the output value changes according to not only the distance from the sensor to the object but also the size or the reflection ratio of the object. For precise detection of the distance, it is effective to calibrate the output value by using a calibration table if it is a known object, or by measuring the size and the reflection ratio in advance with another sensor if it is an unknown object.

The third point is the measurement resolution. The NSPS outputs a continuous analog voltage signal which changes according to the position of the target object. Thus, the measurement resolution of the sensor depends on the resolution of the A/D converter for reading the sensor and the noise on the output signal. Although the noise size differs in the experimental conditions, it has been observed to be less than 1% of the signal in most cases. If the A/D converter has high resolution and sampling rate, the measuring resolution of the sensor can be improved by averaging the successive data. In theory, the resolution, precision and accuracy would improve by arranging the photo-elements more dense, because the amount of the light for sensing. Furthermore, the sensor would be able to detect a smaller object. However, it has to be carefully designed so that the elements do not be saturated
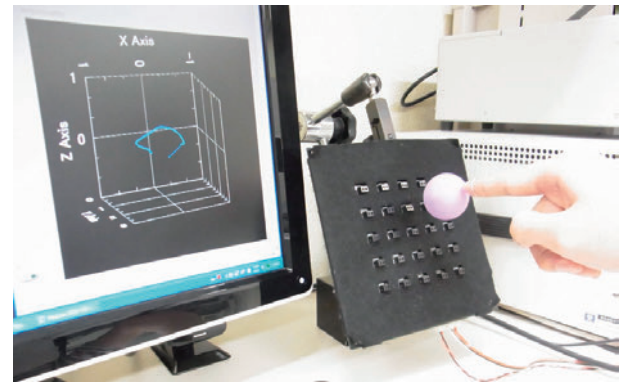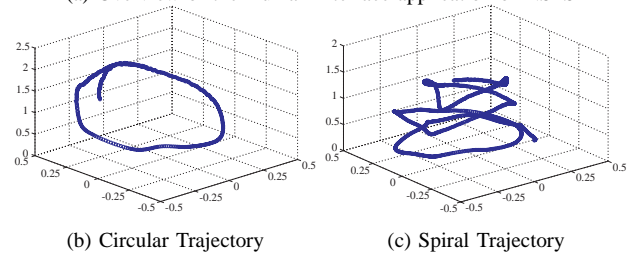
when an object is at the nearest range. On the other hand, the demerit is increase of the power consumption and the production cost.

The fourth point is cross-talk among multiple NSPS. When two or more NSPS are mounted close or face-to-face, such as the case of the robot hand shown in Fig. 1(d), it is necessary that the light emitted from one sensor does not influence the other sensors. In such cases, we should measure the signals with time-sharing processing. This enables each of the sensors to react to the light emitted by itself, without influence of the other sensors. In addition, it is observed to be available to emit the light in a certain frequency and apply a bandpass-filter to the signal.

Finally, we discuss two applications of NSPS to make use of its features, that is, simple structure and high-speed 3D-position detection of the nearby object.

One application is the human interface device as shown in Fig. 12. Figure 12 (a) illustrates the use scene of NSPS for 3D finger trajectory input, (b) and (c) are examples of captured finger trajectories during 1 second. To obtain the 3D coordinates of the object attached on user's fingertip, position outputs of the NSPS x_c, y_c are used directly, z is estimated from the total current output I_{all}. Approximately, I_{all} is inversely proportional to square of the distance to the detected object and is proportional to the area of the orthogonal projection of the object shape to the sensor plane. Based on this characteristics, we determined the object-specific transformation coefficient c by using curve fitting to the distance vs total current output characteristics, and defined the estimation equation as

$$\hat{z} = c \cdot I_{all}^{-2} \qquad (40)$$

where $\hat{z}$ is the estimated value of z position. Here, the coefficient c differs by the size or the reflectance property of the object. Thus, we have to input the information about the
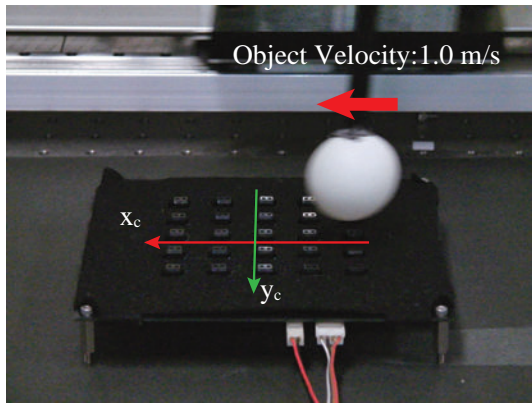
(a) Overall Trajectory of Object x_o and Sensor Output x_c
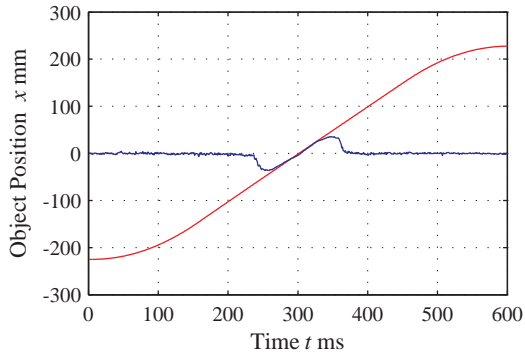
(b) Overall Trajectory of Object x_o and Sensor Output x_c
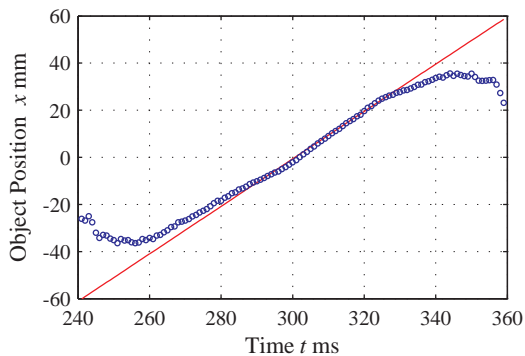
(c) Comparison between the Sensor Output and Object Position while the Object Passes within the Sensing Area

Fig. 13. Object Trajectory vs Sensor output of 1000 mm/s moving target

object preliminary, at the present sensor configuration. We are now developing a method for detecting distance independent of the object size and reflectance, for example, mounting two NSPS with different characteristics for distance detection on the same surface.

The realtime target trajectory measurement by NSPS enables quick gesture input to information devices. Compared with competing methods such as 3D mouse, haptic device and motion-capture, NSPS has the features of high-speed and non-contact sensing. In comparison with 3D mouse and haptic device, NSPS provides unrestrained movements of hands and arms. In comparison with motion-capture based on cameras or depth sensors, it performs overwhelming low output latency. Therefore, NSPS would realize more stress-free

intuitive gesture input than these devices.

The other application is robotics. NSPS achieved high speed response within 1 ms and scalable structure of circuitry that covers from the fingertip to the whole body of a robot. These features, combined with realtime feedback, enable robots to response quickly to the environments, e.g. positioning, attitude and shape adaptive grasping for manipulators, or collision avoidance with moving obstacles for mobile robots. For instance, Fig. 13 demonstrates the response speed to the moving object. The 38 mm diameter white foam polystyrene sphere mounted on the linear slider, passed 10 mm above the surface of NSPS at 1 m/s velocity. Figure 13 (b) and (c) are the comparison between the position output of NSPS x_c and actual positioning of the object x_o derived from the encoder output of the linear motor stage. The object crossed above the sensing area during $t = 260$ ms to 340 ms. The output of the NSPS x_c, y_c and I_{all} are measured at 1 kHz sampling rate, as Fig. 13(c) indicates, the position output x_c tracked the object position withouts significant delay.

For robot hands, in addition, the NSPS covering fingers and palms to contact with grasped objects detects the relative positioning until they contact (i.e., the robot itself occludes the object graped most severely). With previous sensing methods, lack of information by occlusion and limited output response speed made it difficult for robotic manipulators to approach and grasp target objects quickly, the combination of NSPS and simple control law would realize such quick grasping actions.

VII. CONCLUSION

We presented Net-Structured Proximity Sensor that enables high rate, near range object detection. Based on infrared reflective proximity sensor and simple analog calculation circuit, our method efficiently integrate large number of photoreflectors. To verify the principle, we prototyped 5×5 sensor array and examined its basic characteristics of object detection and rapid output response within 1 millisecond. Future work will focus on its practical design for robots such as multifingered hand and mobile robot and evaluating its performance in robotic tasks.

REFERENCES

[1] A. R. Johnston, "Optical proximity sensors for manipulators," Jet Propulsion Laboratory, NASA, Tech. Rep. JPL-TM-33-612, May 1973.
[2] A. Bonen, R. Saad, K. Smith, and B. Benhabib, "A novel electrooptical proximity sensor for robotics: calibration and active sensing," *Robotics and Automation, IEEE Transactions on*, vol. 13, no. 3, pp. 377 –386, jun 1997.
[3] J. Schoenwald, M. Black, J. Martin, G. Arnold, and T. Allison, "Acoustic range sensing servo control: Improved robot positioning and trajectory," *Ultrasonics, Ferroelectrics and Frequency Control, IEEE Transactions on*, vol. 34, no. 2, pp. 225 –231, march 1987.
[4] D. Balek and R. Kelley, "Using gripper mounted infrared proximity sensors for robot feedback control," in *Robotics and Automation. Proceedings. 1985 IEEE International Conference on*, vol. 2, mar 1985, pp. 282 – 287.
[5] S. Walker, K. Loewke, M. Fischer, C. Liu, and J. Salisbury, "An optical fiber proximity sensor for haptic exploration," in *Robotics and Automation, 2007 IEEE International Conference on*, april 2007, pp. 473 –478.
[6] J. Fujimoto, I. Mizuuchi, Y. Sodeyama, K. Yamamoto, N. Muramatsu, S. Ohta, T. Hirose, K. Hongo, K. Okada, and M. Inaba, "Picking up dishes based on active groping with multisensory robot hand," in *Robot and Human Interactive Communication, 2009. RO-MAN 2009. The 18th IEEE International Symposium on*, sep. 2009, pp. 220 –225.

[7] R. Wistort and J. Smith, "Electric field servoing for robotic manipulation," in *Intelligent Robots and Systems, 2008. IROS 2008. IEEE/RSJ International Conference on*, sept. 2008, pp. 494 –499.

[8] B. Mayton, L. LeGrand, and J. Smith, "An electric field pretouch system for grasping and co-manipulation," in *Proc. IEEE Int. Conf. on Robotics and Automation*, 2010, pp. 831–838.

[9] K. Hsiao, P. Nangeroni, M. Huber, A. Saxena, and A. Y. Ng, "Reactive grasping using optical proximity sensors," in *Proc. IEEE Int. Conf. Robotics and Automation ICRA '09*, 2009, pp. 2098–2105.

[10] R. Volpe and R. Ivlev, "A survey and experimental evaluation of proximity sensors for space robotics," in *Proc. IEEE Int. Conf. on Robotics and Automation*, 1994, pp. 3466–3473.

[11] R. Masuda, S. Sasaki, and K. Hasegawa, "Optical proximity sensor by using phase information," *Trans. of the Society of Instrument and Control Engineers*, vol. E-1, no. 1, pp. 6–12, 2001.

[12] L. Marques, U. Nunes, and A. de Almeida, "A new 3d optical triangulation sensor for robotics," in *Advanced Motion Control, 1998. AMC '98-Coimbra., 1998 5th International Workshop on*, jun-1 jul 1998, pp. 512 –517.

[13] H.-K. Lee, S.-I. Chang, and E. Yoon, "Dual-mode capacitive proximity sensor for robot application: Implementation of tactile and proximity sensing capability on a single polymer platform using shared electrodes," *Sensors Journal, IEEE*, vol. 9, no. 12, pp. 1748 –1755, dec. 2009.

[14] H. Kawasaki, T. Komatsu, and K. Uchiyama, "Dexterous anthropomorphic robot hand with distributed tactile sensor: Gifu hand ii," *IEEE/ASME Trans. on Mechatronics*, vol. 7, no. 3, pp. 296–303, 2002.

[15] T. Mukai, M. Onishi, T. Odashima, S. Hirano, and Z. Luo, "Development of the tactile sensor system of a human-interactive robot "RI-MAN"," *IEEE Trans. on Robotics*, vol. 24, no. 2, pp. 505 –512, april 2008.

[16] A. Schmitz, P. Maiolino, M. Maggiali, L. Natale, G. Cannata, and G. Metta, "Methods and technologies for the implementation of large-scale robot tactile sensors," *IEEE Trans. on Robotics*, vol. 27, no. 3, pp. 389–400, 2011.

[17] Y. Ohmura, Y. Kuniyoshi, and A. Nagakubo, "Conformable and scalable tactile sensor skin for curved surfaces," in *Robotics and Automation, 2006. ICRA 2006. Proceedings 2006 IEEE International Conference on*, may 2006, pp. 1348 –1353.

[18] T. Ishihara, A. Namiki, M. Ishikawa, and M. Shimojo, "Dynamic pen spinning using a high-speed multifingered hand with high-speed tactile sensor," in *6th IEEE-RAS Int. Conf. on Humanoid Robots*, 2006, pp. 258–263.

[19] D. Gunji, Y. Mizoguchi, S. Teshigawara, A. Ming, A. Namiki, M. Ishikawa, and M. Shimojo, "Grasping force control of multi-fingered robot hand based on slip detection using tactile sensor," in *IEEE Int. Conf. on Robotics and Automation*, 2008, pp. 2605–2610.

[20] M. Shimojo, T. Araki, A. Ming, and M. Ishikawa, "A high-speed mesh of tactile sensors fitting arbitrary surfaces," *IEEE Sensors J.*, vol. 10, no. 4, pp. 822 –830, 2010.

[21] B. Iske, B. Jager, and U. Ruckert, "A ray-tracing approach for simulating recognition abilities of active infrared sensor arrays," *IEEE Sensors J.*, vol. 4, no. 2, pp. 237–247, 2004.